Dept. of Math. University of Oslo
Mechanics and Applied Mathematics no 01
ISSN 0809–4403 September 2014

A note on instabilities in the boundary layer during runup of solitary waves on a plane slope

Erika K. Lindstrøm, Joris C. G. Verschaeve, Geir K. Pedersen

September 15, 2014

1 Abstract

The present report is concerned with the evolution of boundary layers during runup of solitary waves on a beach in a wave tank of depth 0.2 m. It comprises both theory and high resolution PIV measurements of velocity profiles. A linear stability analysis of the boundary layer for solitary waves running up a sloping beach is performed by means of the Orr-Sommerfeld equation. Due to the increased retardation phase during runup, the amplification of disturbances in the boundary layer is increased as compared to that of solitary waves traveling on constant depth. On the basis of these results, we reexamine the experimental results by Pedersen *et al.* [11] and find some experimental evidence for Tollmien-Schlichting waves destabilizing the flow.

2 Introduction

Runup on waves on inclined planes, with apparent applications to tsunamis and coastal engineering, is a topic which has been studied in a series experimental and theoretical papers over the last 60 years, say. Any kind of review is beyond the scope of this report and we refer to the references given in the papers cited below. In [7, 8] runup on a broken beach was investigated, among other things. For reference also the standard experiment of runup on an inclined plane was revisited. Surprisingly, these experiments yielded much lower runup than theoretical inviscid models. The presence of a viscous boundary layer was apparent, but this was inadequately resolved in the measurements. A new set of experiments, with particular emphasis on shoreline tracking and measurement of viscous boundary layer for solitary waves incident on a beach was performed and published in Pedersen *et al* [11]. In some cases they found very good general agreement between their experimental and numerical velocity profiles in the boundary layer. They also unraveled a delay in the runup, most pronounced for small amplitudes, due to capillary effects. Moreover, the reduced runup heights from [7, 8], as compared to inviscid theories, were reproduced. In [11] this was linked to the viscous effects through integrated mass transport deficiencies and dissipation in the boundary layer, which points to a scale dependency of wave tank experiments of this kind. A survey of the experimental literature also suggested that this was observed before, although being little appreciated.

In some of the experiments reported by Pedersen et al. [11] they observed undulations in the steamline patterns of the boundary layers followed by the development of structures that may be vortex rollers. During withdrawal, when the flow again is accelerated, the boundary layers returned to a regular flow without signs of instabilities or transition. Since no previous analysis or investigation of boundary layers on beaches was available, the authors compared their findings to the related case of boundary layers

under solitary waves for which there is a small number of studies in the literature. In particular, the works by [12, 14, 15, 9] reported the boundary layer stability under solitary waves to be of parametric nature, meaning that the boundary layer turns unstable in an absolute sense beyond a critical Reynolds number. Instabilities did first occur in the retardation phase where an inflection point develops in the boundary layer profile. Since the flow during runup on a beach is a retarded one [11] suggested that it may have similar boundary layer properties and found irregularities for Reynolds numbers of similar magnitudes as [12, 14, 15, 9]

Another line of research was attempted by [2] who subjected the stability of boundary layers under solitons on constant depth to stability analysis by means of an Orr-Sommerfeld type equation. Later [13] has taken this line of approach much further and contested the concept of parametric instability with a critical Reynolds number. The latter reference found, on the basis of a linear stability analysis, that the boundary layer under a solitary wave is convectively unstable, meaning that the boundary layer acts like a broadband amplifier for incoming perturbations. They explained the observation of diverging critical Reynolds numbers found by [12, 14, 15, 9] by the fact that the level of noise in these experiments and direct numerical simulations was uncontrolled and therefore no repeatability of the flow transition could be expected.

The results [13] motivates us for a renewed investigation of the boundary layers during runup. Herein, we shall investigate the stability properties of the boundary layer under solitary waves running up a sloping beach numerically by means of linear stability. In particular we apply the Orr-Sommerfeld equation to the boundary layer profiles computed in [11]. New experiments have not yet been finalized, but the measurements of [11] will be re-processed and interpreted in light of the stability analysis. In particular we seek experimental evidence for the present theoretical results.

The present note is organized as follows. In section 3, a short description of the problem is presented. Following, we explain the basic equations of the present linear stability analysis in section 4. This section also contains the discussion on the theoretical results of the present note. We then turn to the reexamination of the experimental work by Pedersen *et al* [11] in section 5. Next to a short description of the experimental post-processing, the results of the reexamination are discussed in this section. The present note is concluded in section 6.

3 Description of the problem

The set up was defined in [11] and will only be summarized briefly here. A solitary waves with amplitude a is traveling from left to right with speed c in a basin with constant depth $d = 0.2\,\mathrm{m}$ which is then joined by a plane with inclination angle $\theta = 10^\circ$. In the experiments the wave is generated by a piston wave paddle, while it is introduced through initial conditions in the numerical wave models.

The amplitudes of the solitary waves vary between approximately $a/d \sim 0.1$ to $a/d \sim 0.5$. However, most emphasis is put on $a/d = 0.292$ for which we have best measurements. This is also the only amplitude subjected to stability analysis. As shown in the figure we have a coordinate system x, z aligned parallel and normal to the beach, respectively. For use in the boundary layer computations the x axis is construed to follow also the flat part of the bottom, still with z denoting the normal direction, which then is vertical. In addition we have a horizontal/vertical ξ, ζ system. The origin of both systems are located at the equilibrium shoreline. Some features of the setup are shown in figure 1. In the discussion of the stability theory we will use rescaled, non-dimensional, coordinates. Elsewhere units will generally be applied, or the scaling explicitly stated (such as $a/d \approx 0.3$).

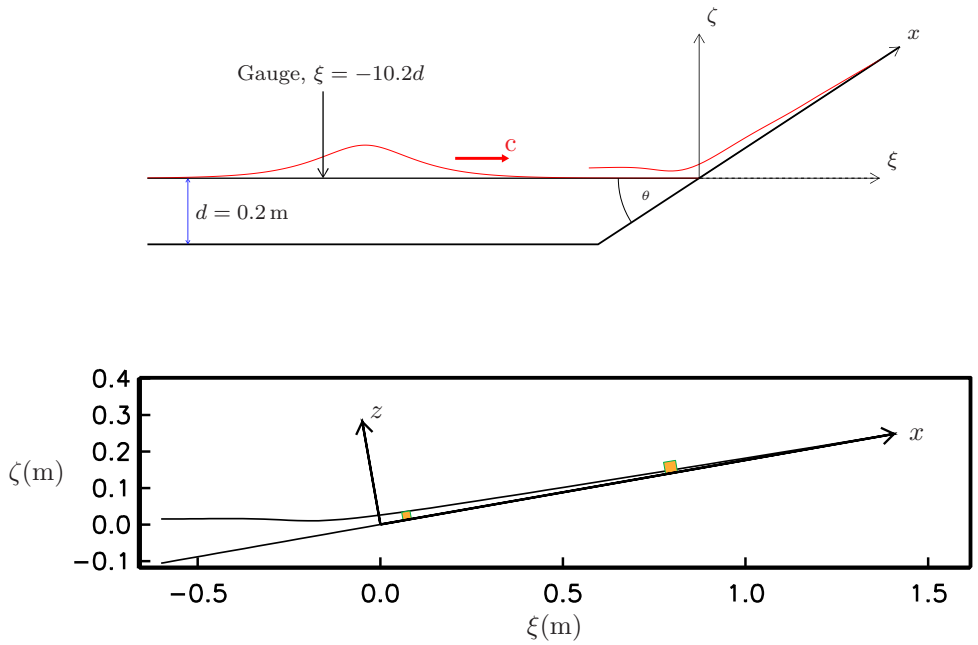

Figure 1: Sketch of problem. Upper panel: Side view of wave tank with the initial wave and the surface at maximum runup as obtained from an inviscid model for $a/d \sim 0.3$. The time series from the gauge is used to synchronize experiments and theory. Lower panel: the swash zone at maximum runup for $a/d \sim 0.3$ with true aspect ratio. The lower and upper rectangles are FOV 2 and 3, respectively. FOV 1 is located in mid-tank in about the same position as FOV 2.

At $\xi = -d/\tan\theta$, the plane beach is installed. When the solitary wave reaches this points it will start to produce a gentle reflection, which will mildly influence the properties of the boundary layers close to the start of the beach. During shoaling the front will steepen, yielding a shorter and stronger acceleration phase as compared to retardation phase. When the solitary wave reaches the shoreline, it will develop a thin swash tongue running up the beach(see lower panel of figure 1) . Gravity will decelerate and then reverse the flow. The flow is first reversed close to the $\xi = 0$ and finally at the moving shoreline when the maximum runup height is reached. The flow is then reversed everywhere reverse and the draw down phase starts. Figure 2 shows a time series of the free stream velocity U_{inviscid} of the boundary layer for the positions in figure 3. The typical free stream velocity of a solitary wave in the constant-depth part of the tank displays an acceleration phase followed by a retardation phase in a symmetrical fashion. In the lowest part of the swash zone a short acceleration phase is followed by a longer retardation which then is conceived as acceleration again as the flow is reversed. Further up the beach the initial acceleration phase is missing and the deceleration phase is even stronger. The larger velocities and stronger retardation during runup must be expected to increase the amplification of perturbations in the boundary layer, destabilizing the flow, as compared to the propagation on constant depth. This boundary layer was investigated by Pedersen *et al.* [11], who solved the boundary layer equations numerically, with outer flows taken from numerical solutions of inviscid wave models. In addition they performed PIV measurements of the boundary layer flow at selected positions as indicated in figure 1. As mentioned in the introduction, the theoretical and experimental profiles were agreeing well, except for some cases, where instabilities were observed to change the flow pattern. The investigation of the stability properties of the boundary layer flow is the focus of the present work, which can be considered a continuation of the work by Pedersen *et al.* [11]. We shall first perform some theoretical considerations, section 4, before turning to the reexamination of the PIV measurements at the locations

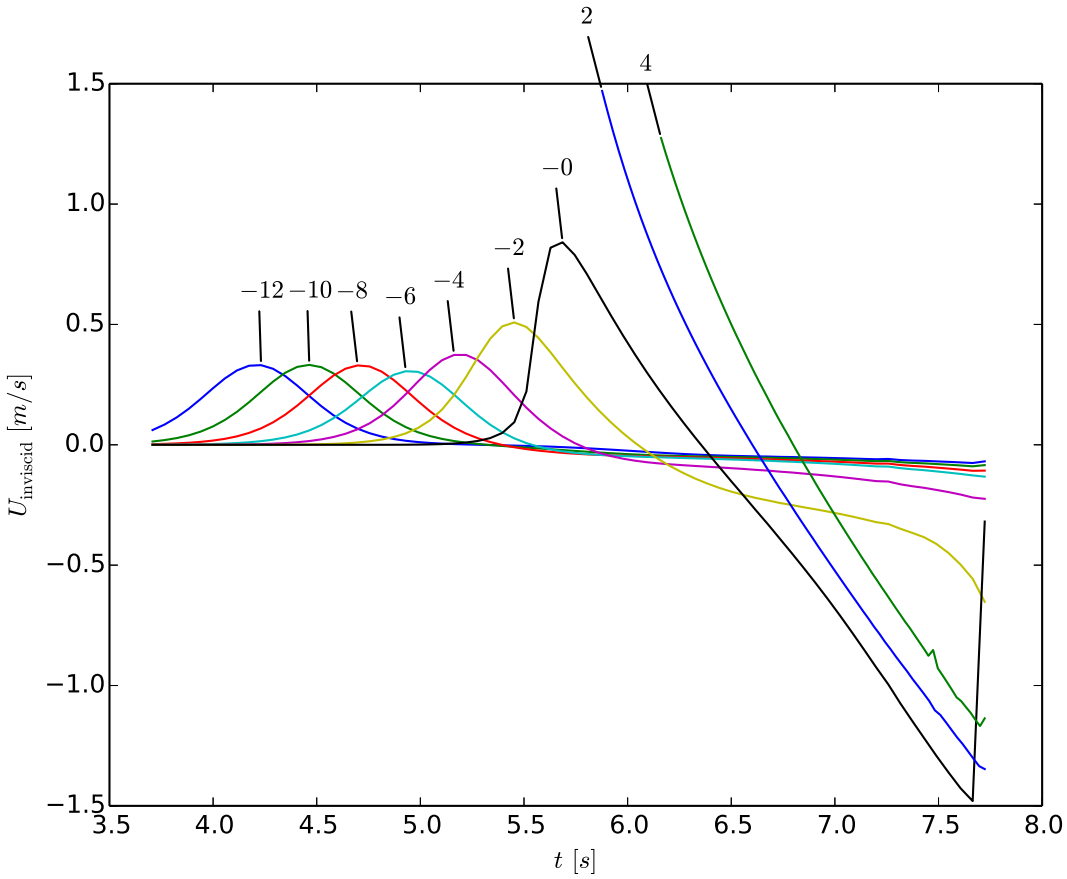

Figure 2: Free stream velocity for different values of ξ^*/d in finite depth and onshore.

in figure 1, cf. section 5.

4 Theory

4.1 Basic equations

In [11], the boundary layer flow under a solitary wave running up a sloping beach was solved numerically. We shall use this solution to perform a stability analysis by means of the Orr-Sommerfeld equation. The solution of the boundary layer equations in [11], leads to a velocity field

$$U_{\text{bl}}(x, y, t) \quad V_{\text{bl}}(x, y, t), \tag{1}$$

in the boundary layer, which is the subject of the present linear stability analysis.

The scaling of quantities in equation (1) is the following. The velocities in tangential and wall normal direction are scaled by the shallow water speed $\sqrt{gd}$. Time is scaled by $d/\sqrt{gd}$ and horizontal lengths are scaled by d. On the other hand, wall normal lengths are scaled by δ^*, where δ^* is a viscous length scale defined in [14, 15]:

$$\delta^* = \sqrt{\frac{2\nu d}{\sqrt{gd}}}. \tag{2}$$

The scale δ^* allows for a non-dimensional small parameter $\delta = \delta^*/d$, which equals for the present flow

depth:

$$\delta = 2.67 \cdot 10^{-3}. \tag{3}$$

The Reynolds number Re for a scaling based on δ^* and $\sqrt{gd}$ is given by:

$$\mathrm{Re} = \frac{2}{\delta}. \tag{4}$$

In equation (1) the components are tangential and normal to the bottom. Hence, for $x^* < -d/\sin\theta$, cf. figure 1, the tangential coordinate is given by ξ, whereas the normal coordinate is given by ζ. Thus, the coordinate system for the boundary layer analysis thus always follows the bottom of the wave tank. The flow defined by (1) is time dependent which necessitates some specification about the exact sense of instability in the present case, since traditionally instability is defined as the departure from one steady solution to another flow regime. The meaning of instability employed here is akin to the concept of spatial growth for a steady boundary layer [6]. For spatial growth, the boundary layer flow is characterized by slow horizontal change, whereas the perturbation displays a rapid variation in the horizontal direction. This concept of two scales, a slow scale for the base flow and a fast one for the perturbation, is in the present note applied to the temporal variation of the flow. The resulting formulation is equivalent to the one in [1]. Given a position x_0 along the beach, the boundary layer flow can be regarded as a succession of slowly varying profiles in z. The stream function ψ' of a Tollmien-Schlichting wave with wave number α can then be written as:

$$\psi' = \phi(y) \exp\{\mathrm{i}\alpha x - \omega t\}, \tag{5}$$

where ϕ is a shape function in wall normal direction. The imaginary part of the complex number ω gives us the frequency of the perturbation, whereas the real part stands for the growth rate of the perturbation. The Tollmien-Schlichting wave displays fast variation compared to the base flow. However, the quantities ϕ and ω are assumed to vary on the same scale as the base flow. The governing equation for ψ' is the celebrated Orr-Sommerfeld equation [3]:

$$\frac{1}{\mathrm{Re}} \left(D^2 - \alpha^2\right)^2 \phi - (\mathrm{i}\alpha U_{\mathrm{bl}} - \omega) \left(D^2 - \alpha^2\right) \phi + \mathrm{i}\alpha D^2 U_{\mathrm{bl}} \phi = 0, \tag{6}$$

where $D = d/dz$. In contrast to the traditional solution of (6), the flow field is not varied in x, but in t, that means, we fix a certain position x_0 and apply equation (6) on a series of profiles for t. Equation (6) is an eigenvalue problem for the eigenvalue ω and the eigenvector ϕ. The boundary layer flow becomes unstable, as soon as the real part of ω for any wave number α becomes positive. The region in the (t, α) plane for which the real part of ω vanishes is called the neutral curve. It separates the stable from the unstable region. In addition to the neutral curve, the total amplification of the Tollmien-Schlichting wave is of major interest, as it tells us by which factor the perturbation will grow during the passage of the solitary wave. The amplification A/A_0 is computed by the following formula:

$$\frac{A}{A_0} = \exp \int_{t_0}^{t} \mathrm{real}\,(\omega)\ dt. \tag{7}$$

Equation (6) is solved by means of a Chebyshev collocation method as in [13], with 130 nodes in y direction. The following section presents the results of the above Orr-Sommerfeld analysis applied to the boundary layer flow in [11].

4.2 Results

The Orr-Sommerfeld equation, equation (6), is solved for a number of positions along the boundary. In the following, we denote each position by its horizontal distance ξ from the origin. The value of the abscissa x on the beach is then obtained by

$$x = \frac{\xi}{\cos\theta}. \tag{8}$$

In figure 3, the neutral curves in the (t, α) for these positions are plotted. When the solitary wave is still propagating on constant depth (for $\xi < -1/\tan\theta \approx -5.67$), the shape of the neutral curve for early times is close to the one for a solitary wave traveling in an infinite basin of constant depth d [13]. The neutral curve starts behind the crest of the solitary wave, where the external flow is decelerating and the resulting external pressure gradient causes the flow in the boundary layer to reverse. However, for later times, the shape of the neutral curves differs from the one of a solitary wave in an infinite basin. The neutral curve reconnects and forms a closed curve much earlier in time. This is due to the reflection of the solitary wave on the beach, which leads to a wave (different in amplitude and shape) traveling the opposite direction, i.e. from right to left. This wave is again characterized by an initial acceleration phase, which stabilizes the flow and leads to an earlier closure of the neutral curve for positions further away from the beach.

For positions on the beach, we see a continuous evolution of the shape of the unstable region. Its extent in time decreases until the equilibrium shoreline $\xi = 0$, when its duration starts to increase again. The span in wave numbers α increases for increasing ξ. For later times the neutral curve develops a kind of bump for $\xi \geq 2$. Even if the neutral curves in the boundary layer of a solitary wave running up a sloping beach display some evolution when compared to the neutral curve for a solitary wave propagating on constant infinite depth, the most dramatic change is in the amplification of the perturbations. In figure 4 top, the amplification of the critical Tollmien-Schlichting waves is plotted for the positions defined in figure 3. Far from the beach, the amplification of the critical Tollmien-Schlichting wave corresponds basically to the one of a solitary wave traveling in an infinitely long basin. However as we approach the shoreline, the maximum amplification decreases, only to show a strong increase towards the end of the swash tongue. This indicates that the stability features in the boundary layer of the swash tongue differ significantly from those of the boundary layer under a solitary wave traveling on constant depth. Further evidence can be obtained by looking at the phase speed of the critical Tollmien-Schlichting wave, cf. figure 4 bottom. Since the Tollmien-Schlichting wave is advected by the flow in the boundary layer, its phase speed reflects qualitatively the boundary layer flow. Far from the beach, we observe first an acceleration of the Tollmien-Schlichting wave before the wave decelerates and moves in opposite direction. This pattern is slowly varied when moving towards the beach with the acceleration phase becoming shorter. Further up the beach $\xi = 2, 4$, the acceleration phase is even completely missing and we only observe a deceleration phase in the beginning. For later times we observe a strong acceleration of the Tollmien-Schlichting wave down the beach. We remark that the very vicinity of the moving shoreline our solution is not correct. Firstly, the wave model from [11] do not include surface tension which will modify the dynamics of the shoreline (contact point). Secondly, the abrupt on-set of the outer flow when a given x position is inundated causes numerical large numerical errors locally.

5 Experimental work

In the present section we employ dimensional quantities, while omitting any stars.

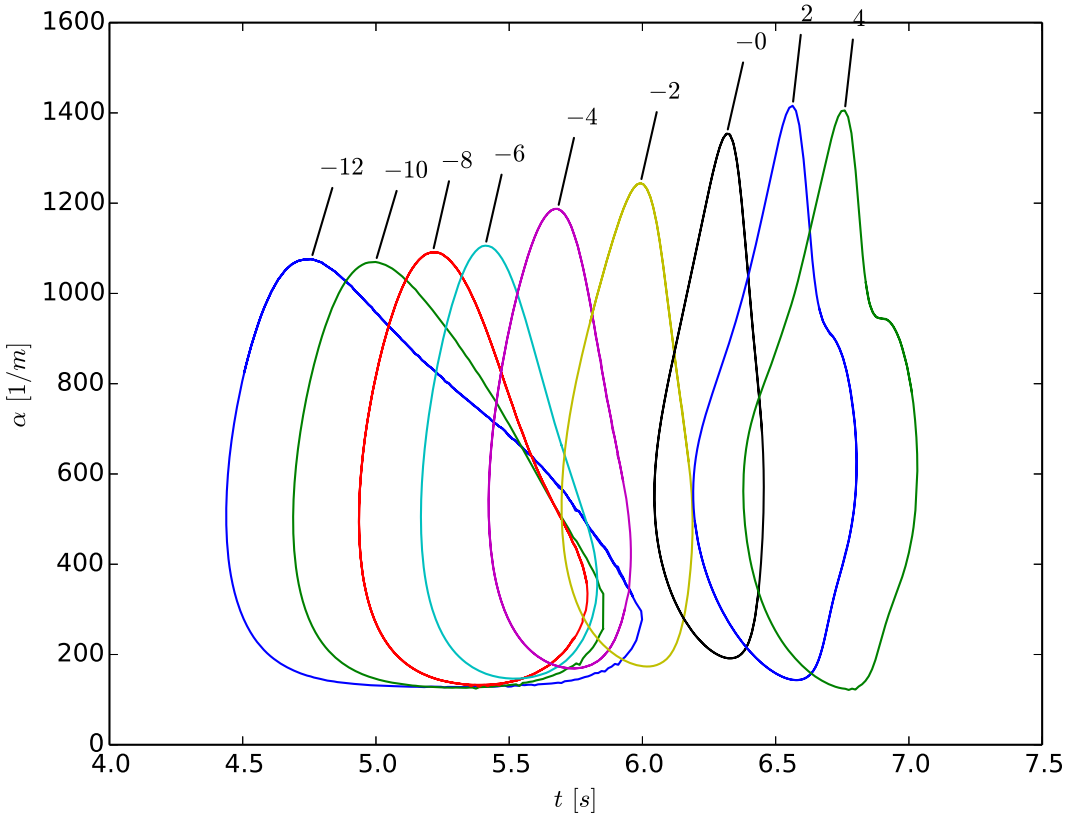

Figure 3: Neutral curves in the (t, α) plane for the boundary layer flow in [11]. The curves are computed for different values of ξ^*/d, which is annotated as a label to the respective curve in the figure.

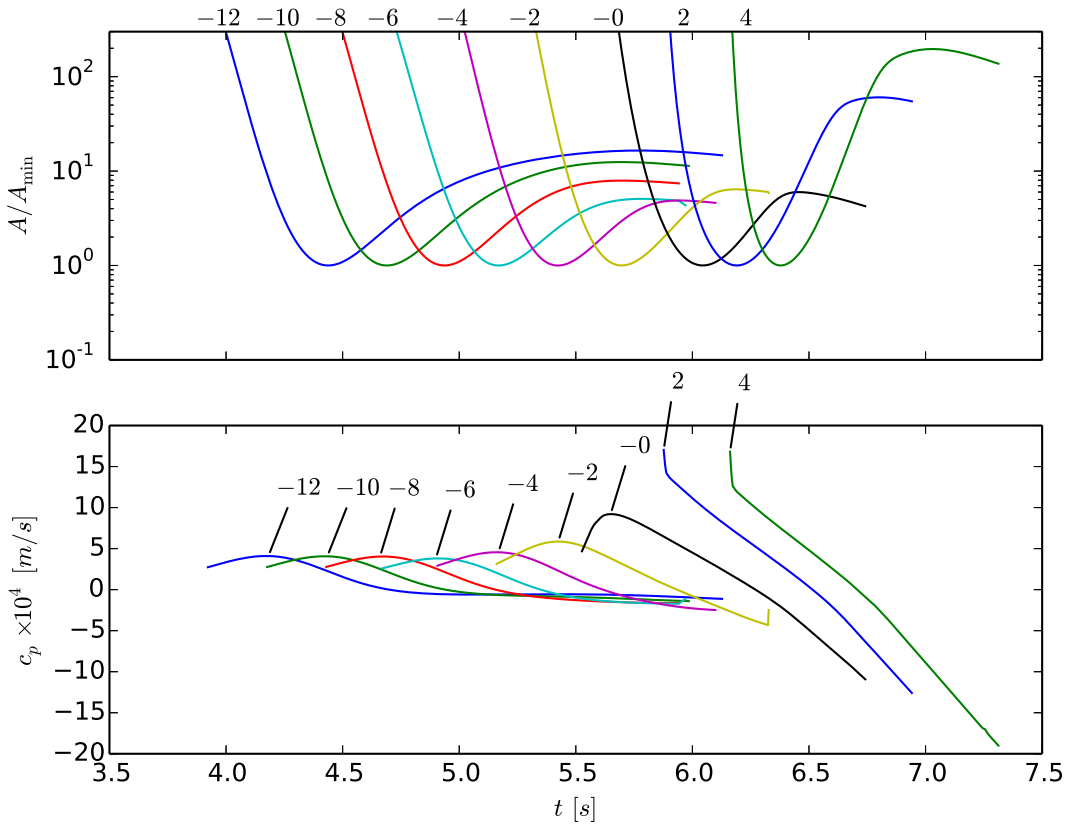

Figure 4: Top: Amplifications of the critical Tollmien-Schlichting waves in figure 3. Bottom: Phase speed of the critical Tollmien-Schlichting waves. Curves are marked with $\xi^\star/d$.

5.1 Experimental setup and instrumentation

Experiments were performed in a wavetank with length 25 m, width 0.51 m and depth 1 m. Both the walls and the bottom is made of glass, suitable for optical measuring techniques. A plane beach of 10° inclination was installed with the undisturbed shoreline located 7.1 m from the wave paddle. The incident solitary waves were generated by a piston type wave paddle by a modified "Goring's method", which is explained in [5]. The generated waves had the amplitudes $a/d = 0.0977, 0.195, 0.292, 0.388, 0.481$. A non-intrusive acoustic wave gauge (Banner U-Gage S 18U) was employed to measure the incident waves at a distance of 2.045 m from the equilibrium shoreline. This gauge was also used to monitor the equilibrium depth.

A PIV (particle image velocimetry) system was used to measure the velocity fields at the beach. Three field of views (FOV) were employed in in the work by PAL, one FOV was placed in the middle of the tank (25 cm from the side wall), 8 cm from the shoreline and with a window size of 5.6 cm × 5.6 cm. Two of them were located 5 cm from the side wall closest to the camera, placed 7.5 cm and 81 cm from the equilibrium shoreline position. These had window size of 2.3 cm × 2.3 cm and 3.3 cm × 3.3 cm respectively. The camera was aligned parallel to the beach, with resolution of 1024 × 1024 pixels and 2000-5000 frames per second. Wave gauges and PIV system was synchronized with the wave paddle, with $t = 0$ as the start of the paddle motion. A more detailed description of the experimental setup and instrumentation are found in [11].

5.2 Post-processing

The main purpose of the investigation in 2013 was to determine the cause of reduced runup heights in experiments compared to numerical models. Irregularities in the flow were detected in the upper FOV as well as in the lower FOV located in the middle of the wave tank. The main focus in the present work is to reanalyze the fluctuations in the flow in the upper FOV. Here, we apply a different kind of filtering to reveal some more details regarding these irregularities. Our main attention is given to the case $a/d = 0.292$. and especially the second of the three runs (Run 2). There is no strict repeatability considering amplitudes and time range of the detected irregularities and Run 2 displays the most distinct and regular oscillations in the flow pattern. Run 2 is also the one with the best seeding and, hence, the most accurate measurements. However, the difference in the measurement quality is probably not the sole reason for the differences between the experiments. For Run 1 and Run 3 the oscillations lasted for a shorter time, in addition to being less distinct. Both spatial and temporal resolution is considered for Run 2 while only spatial resolution is applied for Run 1 and Run 3.

To reduce noise, the data is averaged over 0.003 s in time and 0.02 mm in x. We note that the averaging period is smaller than in [11], where 0.01 s was applied. Figure 5 shows the filtered data where the fluctuations are visible. In order to extract perturbations from velocities, the horizontal velocity component is separated into a base flow, which is approximated as a linear function $u_0 + u_1 x$, and perturbations u_p:

$$u = u_0 + u_1 x + u_p \tag{9}$$

In order to verify the linear approximation of the base flow, it is compared with theoretical computations at the same position and time regime for nonlinear boundary layers which display a L2 norm of residuals in order of 10^{-5} m/s for spatial resolution and 10^{-3} m/s for temporal resolution. Figure 6 shows the original data, u, and the perturbations, u_p, from run 2 at $z = 1.9$ mm for $t = 6.43$ s in spatial resolution and $x = 0.807$ m for temporal resolution.

In addition the seeding in Run 1 and Run 3 were less dense than for Run 2, which resulted in reduced quality of the processed data due to lack of valid velocity vectors.

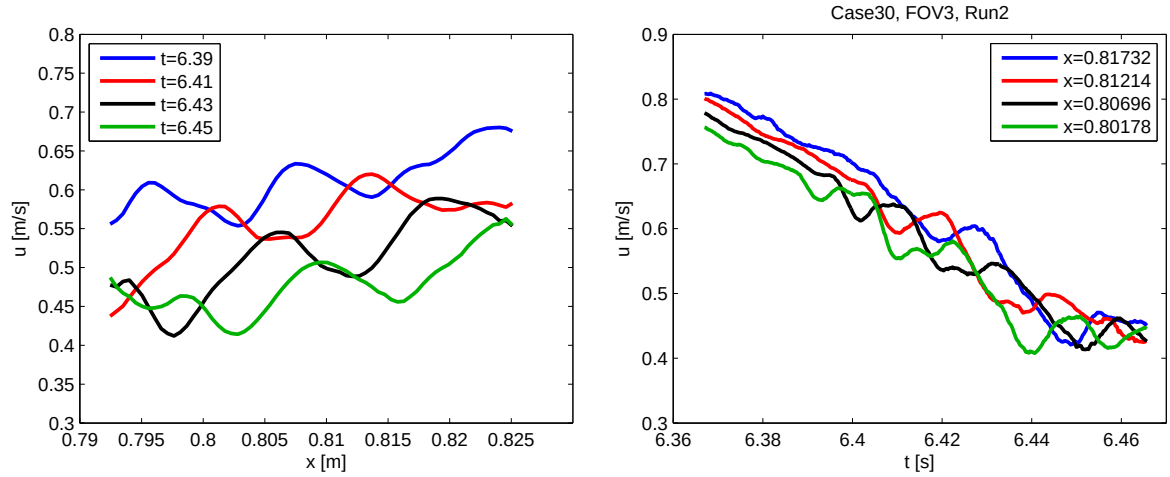

Figure 5: Detected irregularities in space (left) and time (right). $a/d = 0.292$ Run 2.

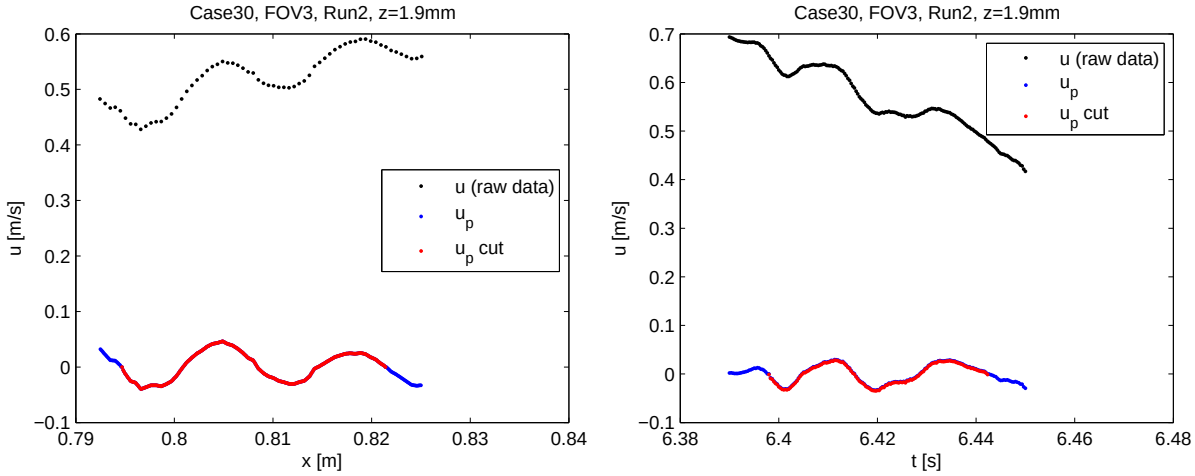

Figure 6: Horizontal velocity component u, perturbations, u_p, and selected sequence for the Fourier transformation, $u_p cut$. Data from $z = 1.9\,\mathrm{mm}$. Left: Spatial resolution, $t = 6.43\,\mathrm{s}$. Right: Temporal resolution, $x = 0.807\,\mathrm{m}$. $a/d = 0.292$ Run2.

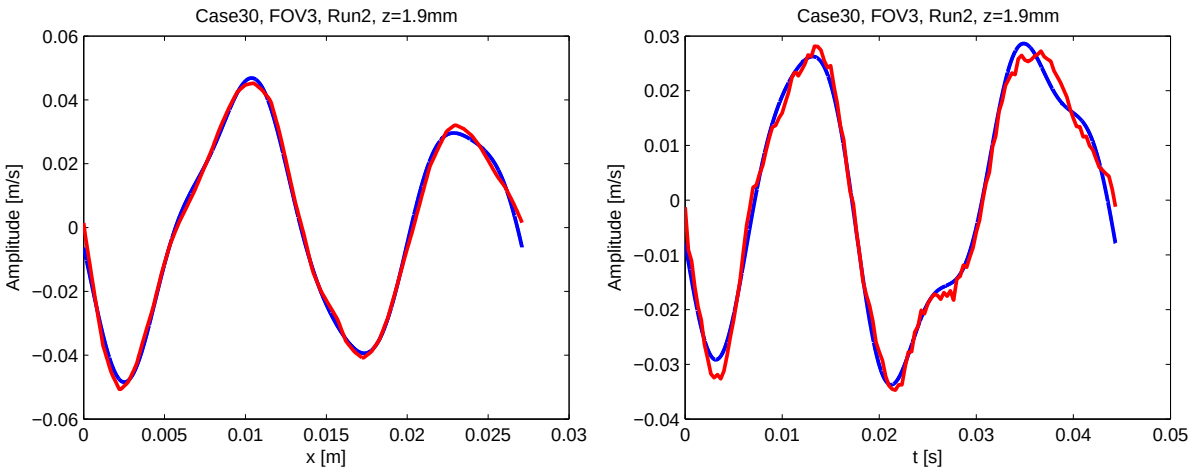

Figure 7: Perturbations plotted in red and Fourier approximation of the signal plotted in blue at $z = 1.9\,\text{mm}$. Left: Spatial resolution, $t = 6.43\,\text{s}$. Left: Temporal resolution, $x = 0.807\,\text{m}$. $a/d = 0.292$ Run 2.

Once the perturbations are extracted from the data, the first and last zero-crossings of the perturbations within the FOV are found and Fourier transformation is applied within the interval confined by the zero crossings. Thus, the chosen domain will determine the wavelengths in the Fourier transformation. This method is crude, and one must keep in mind that the length of the chosen sequence will vary in time or space for spatial or temporal resolution respectively. As a consequence of this is that the components of the Fourier transformation will also vary. Figure 7 shows the selected sequence, denoted u_{cut}, and the first five terms of the corresponding Fourier transformation for run 2 at $t = 6.43\,\text{s}$ and $x = 0.807\,\text{m}$.

Amplitudes of the Fourier components are normalized with the outer velocity of the flow. The outer flow is extracted from the PIV data at $z = 6.5\,\text{mm}$. There are drop outs in the outer flow, caused by poor seeding. Due to this, the outer flow velocity is taken as the median (mean of the middle two numbers in sorted order) over the chosen sequence for each time frame in spatial resolution and for each x-position in temporal resolution. For spatial resolution, the outer flow vary slightly within the FOV for each time frame, with maximum variation of 3%. Variation of the outer flow in temporal resolution is larger, with a maximum of 25%.

When possible, wavelengths or periods of the oscillations are found from visual inspection (no mathematical interpolation involved) of all the zero crossings of the perturbations within the FOV or time range considered. The method is to extract the distance between zero crossings covering one wavelength, for all wavelengths within the chosen sequence. The final estimate for the wavelength is then the average of all distances found within the sequence. This method is even more crude and are used for comparison to the Fourier transformation.

5.3 Experimental observations

5.3.1 Results of $a/d = 0.292$, Run 2

Figure 9-11 shows streamlines at different stages of the flow during run up and draw down, while figure 12 shows the corresponding horizontal velocity component, u, at $z = 1.9\,\text{mm}$. No irregularities are noticeable in the early stage of the run up, then small fluctuations occur which develop to what might be related to Tollmien Schlichting waves. These waves are regular for a very short time before the oscillations become more irregular, followed by formation of vortices in the boundary layer which seems to be transported outwards. Irregularities are not visible during draw back. The most regular oscillations

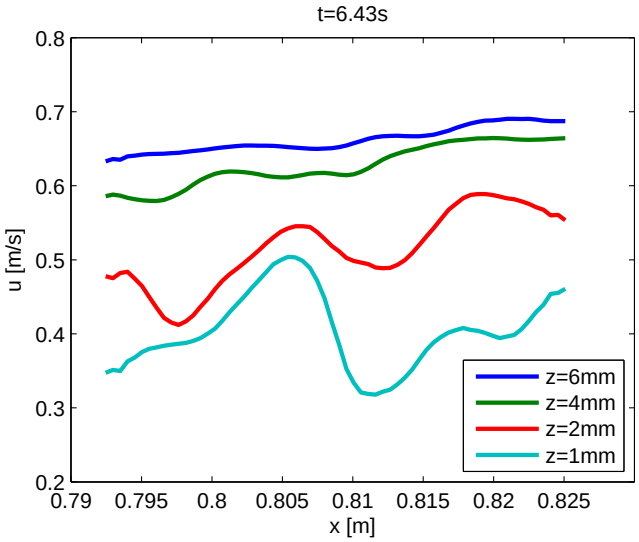

Figure 8: $a/d = 0.292$ Run 2. Horizontal velocity u for $z = 1, 2, 4$ and 6 mm at $t = 6.43$ s

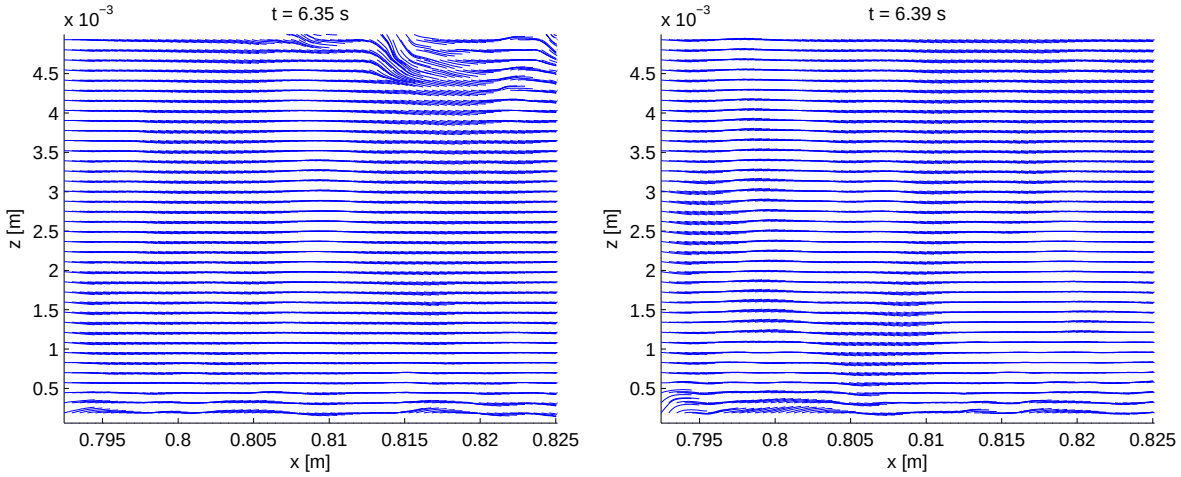

Figure 9: Streamlines extracted from $a/d = 0.292$ Run 2. Left image, $t = 6.35$ s, shows the early stage of run up with no sign of fluctuations, the irregularities in the upper right is caused by lack of seeding. Right image, $t = 6.39$ s shows the streamlines when fluctuations occur.

are detected in run 2 at $z = 1.9$ mm, as seen in figure 8 where the horizontal velocity component of the flow for $z = 1, 2, 4$ and 6 mm is shown.

Figure 13 shows wave numbers k_i, $i = 0, 1, 2, 3, 4$, together with corresponding amplitudes for $t = 6.37$, 6.41, 6.43 and 6.46 s. The amplitudes are normalized with the outer flow which is extracted from the PIV data. Inspection of amplitudes of the Fourier components reveals that k_1 is the dominant component of the perturbations. Temporal evolution of amplitudes for k_1-k_4 are shown in figure 14.

A phase of strong growth in A_1 is evident for t between $t = 6.38$ s and $t = 6.43$, say. Since we do not have any knowledge of "initial amplitudes" in the experiments the amplitudes themselves cannot be related to theory, but times and relative growth rates, $A^{-1}\mathrm{d}A/\mathrm{d}t$, can be compared. It is remarkable that for the given position the theory (figure 4, $\xi/d = 4$) predicts $t_c = 6.38$ s (critical time of instability when A starts to grow). However, while the growth in the experiment takes place in the range 6.38 s − 6.43 s, with a relative growth rate of 80 s^{-1} in the first part of this range, the growth in the theory lasts until $t = 6.9$ s, with a maximum relative growth rate of 15.7 s^{-1} at $t = 6.66$ s. Naturally, the estimates of the growth rates

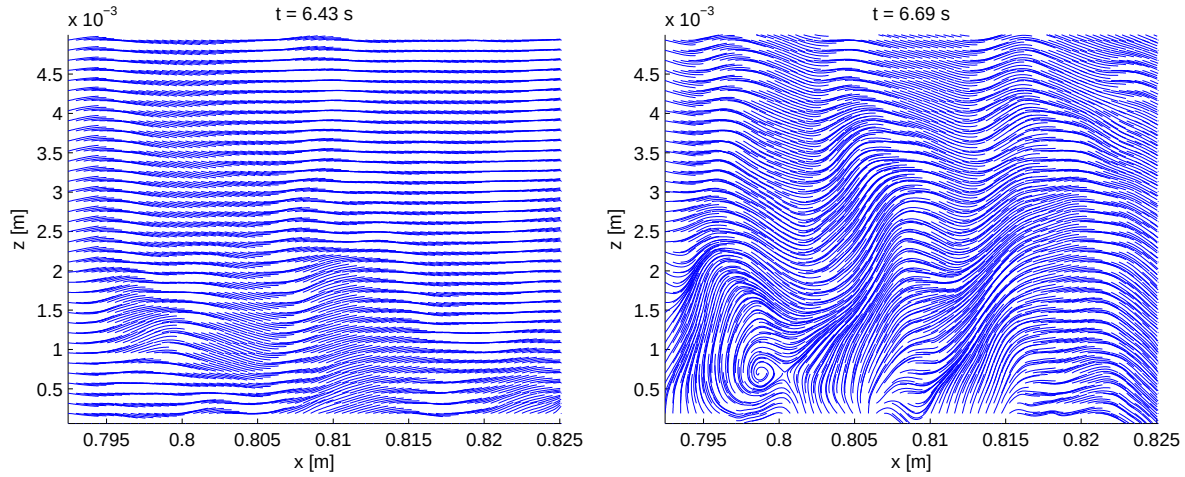

Figure 10: Streamlines extracted from $a/d = 0.292$ Run 2. Left image, $t = 6.43\,\mathrm{s}$, shows the streamlines when the Tollmien Schlichting waves appear in the flow. Right image, $t = 6.69\,\mathrm{s}$ shows the first generated vortex.

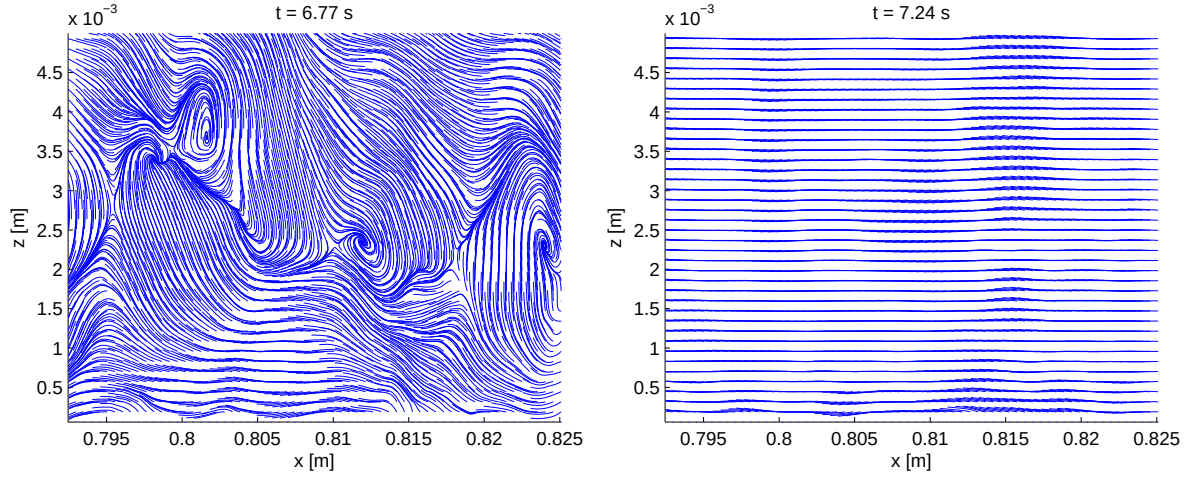

Figure 11: Streamlines extracted from $a/d = 0.292$ Run 2. Left image, $t = 6.77\,\mathrm{s}$, Vortices are transported outwards. Right image, $t = 7.24\,\mathrm{s}$ no sign of irregularities during draw back.

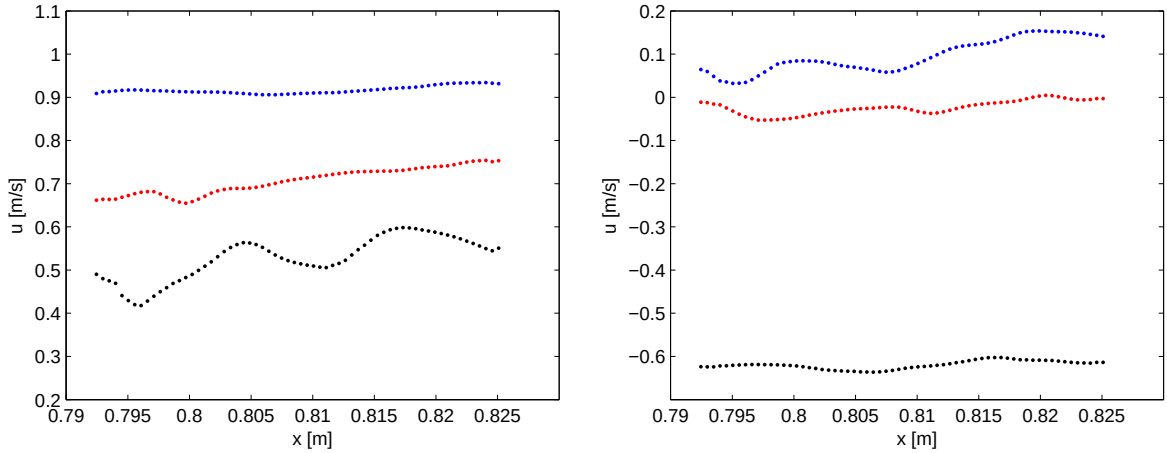

Figure 12: Velocities extracted from $a/d = 0.292$ Run 2. Left image: horizontal velocity component u, $t = 6.31\,\mathrm{s}$, $t = 6.39\,\mathrm{s}$ and $t = 6.43\,\mathrm{s}$ in blue, red and black. Right image: $t = 6.69\,\mathrm{s}$, $t = 6.77\,\mathrm{s}$ and $t = 7.24\,\mathrm{s}$ in blue, red and black.

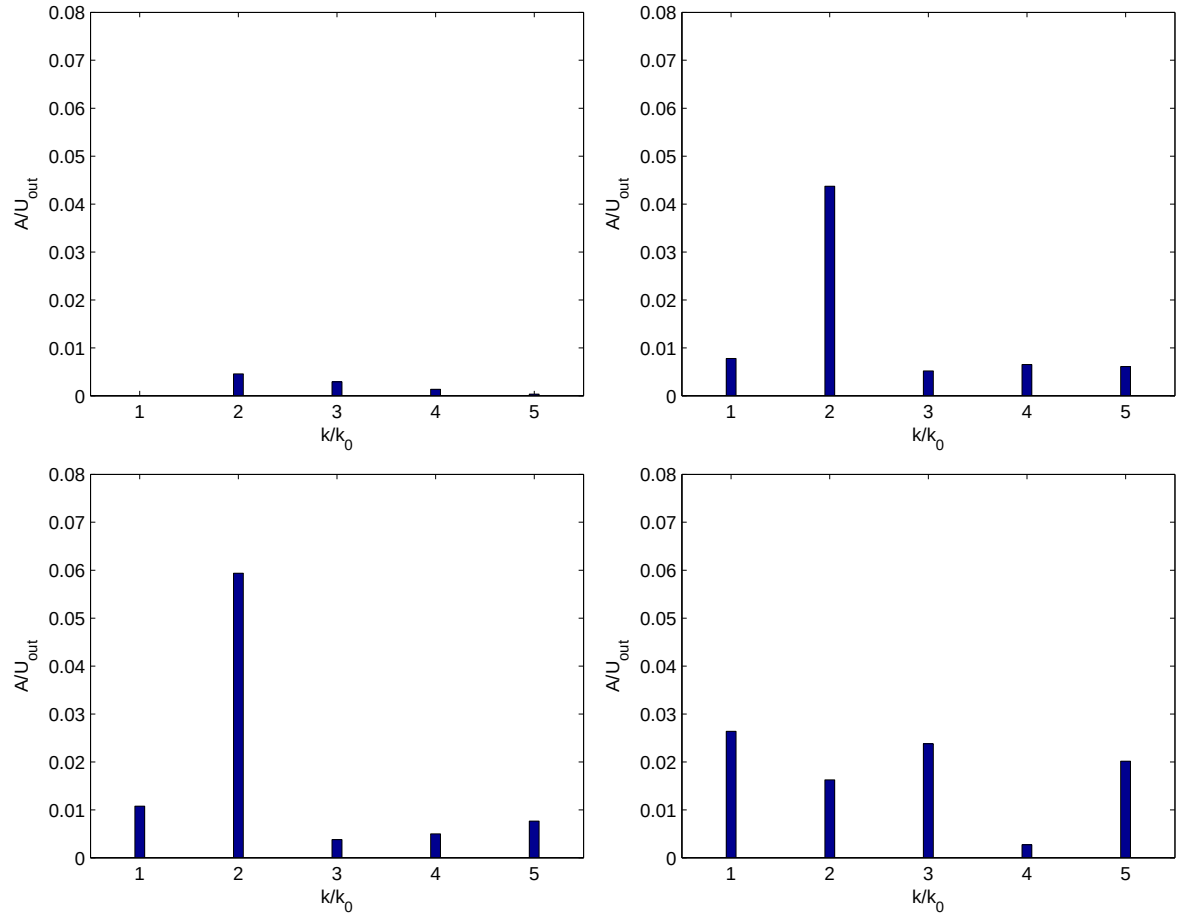

Figure 13: $a/d = 0.292$ Run 2. Wave numbers k_i, $i = 0 : 4$ with increasing k from left to right and corresponding amplitudes of the perturbations at $t = 6.37\,\mathrm{s}$ upper left, $t = 6.39\,\mathrm{s}$ upper right, $t = 6.43\,\mathrm{s}$ lower left, $t = 6.46\,\mathrm{s}$ lower right.

in the experiments are inaccurate. According to figure 10 in [10] there may also be significant differences in the base flows (boundary layer profiles before instability becomes noticeable) between experiments and theory. A difference must be assumed since the experimental and theoretical/inviscid runup height differs by 20% and FOV 2 is close to the shoreline (see figure 1). Still, the differences concerning growth rate are so substantial that we cannot rule out the possibility that the rapid experimental transition around $t = 6.40\,\mathrm{s}$ may be a secondary instability and that the first linear instability is lost in the measurements. According to [4] a secondary instability may be expected when the magnitude of undulations reaches, say, 1% of that of the base flow, while we measure the strong growth rates when the amplitudes are between 1% and 5% of the base flow.

Wavelengths, λ_1-λ_4, are shown in figure 15. Eddies that are formed in the later stage are shown in figure 16. The average distance measured between two consecutive eddies, shown in the figure, is $5 \times 10^{-3}\,\mathrm{m}$. Wavelengths, λ_1, are given in table 1 together with amplitudes of the perturbations, outer velocities and wavelengths, λ_{viz}, that are found by purely visual inspection. Wavelengths λ_1 vary between 1.01 cm and 1.57 cm, while the critical wave number extracted from the theoretical neutral curve corresponds to a wavelength of 1.05 cm. Hence, the length of first unstable mode in the analysis is clearly of the same order as the lengths observed in the experiment. Results from the temporal resolution are given in table 2, where periods T_1 are listed together with amplitudes of the perturbations, outer velocity and periods T_{viz} that are found by visual inspection.

Time	k_0 $[m^{-1}]$	λ_1 $[m]$	λ_{viz} $[m]$	u_{out} $[m/s]$	A_1/u_{out}
6.37 s	2.40×10^2	1.31×10^{-2}	-	7.94×10^{-1}	0.46×10^{-2}
6.38 s	2.12×10^2	1.49×10^{-2}	-	7.74×10^{-1}	0.28×10^{-2}
6.39 s	3.10×10^2	1.01×10^{-2}	-	7.48×10^{-1}	0.80×10^{-2}
6.40 s	2.13×10^2	1.47×10^{-2}	-	7.23×10^{-1}	1.94×10^{-2}
6.41 s	2.59×10^2	1.21×10^{-2}	1.2×10^{-2}	6.92×10^{-1}	4.37×10^{-2}
6.42 s	2.12×10^2	1.49×10^{-2}	1.2×10^{-2}	6.72×10^{-1}	4.25×10^{-2}
6.43 s	2.32×10^2	1.36×10^{-2}	1.4×10^{-2}	6.62×10^{-1}	5.94×10^{-2}
6.44 s	2.01×10^2	1.57×10^{-2}	1.4×10^{-2}	6.35×10^{-1}	4.63×10^{-2}
6.45 s	2.33×10^2	1.36×10^{-2}	-	6.19×10^{-1}	2.55×10^{-2}
6.46 s	2.05×10^2	1.54×10^{-2}	-	6.02×10^{-1}	1.63×10^{-2}

Table 1: $a/d = 0.292$ Run 2. Wave numbers k_0 and wavelengths λ_1 extracted from Fourier transformation, wavelengths λ_{viz} extracted manually from the figures, outer velocity u_{out} and amplitude A_1/u_{out}

x $[m]$	ω_0 $[rad/s]$	T_1 $[s]$	T_{viz} $[s]$	u_{out} $[m/s]$	A_1/u_{out}
0.800	1.30×10^2	2.42×10^{-2}	-	6.71×10^{-1}	5.1×10^{-2}
0.802	1.30×10^2	2.42×10^{-2}	-	6.62×10^{-1}	5.1×10^{-2}
0.803	1.30×10^2	2.42×10^{-2}	3.0×10^{-2}	6.56×10^{-1}	4.93×10^{-2}
0.805	1.06×10^2	2.95×10^{-2}	2.4×10^{-2}	6.74×10^{-1}	2.98×10^{-2}
0.807	1.42×10^2	2.22×10^{-2}	2.6×10^{-2}	6.79×10^{-1}	3.77×10^{-2}
0.815	1.30×10^2	2.42×10^{-2}	2.6×10^{-2}	6.95×10^{-1}	3.52×10^{-2}
0.816	1.23×10^2	2.55×10^{-2}	2.8×10^{-2}	6.99×10^{-1}	3.40×10^{-2}

Table 2: $a/d = 0.292$ Run 2. Angular frequencies ω_0 and periods T_1 extracted from Fourier transformation, periods, T_{viz} extracted manually from the figures, outer velocity u_{out} and amplitude A_1/u_{out}

5.3.2 Brief overview of $a/d = 0.292$, Run 1 and Run 3

Results from the spatial resolution is extracted from the data for Run 1 and Run 3 and given in tables 3 and 4. Amplitudes of the perturbations are markedly smaller in Run 1 compared to Run 2, while for Run 3 the amplitudes are comparable to those of Run 2. One should also notice that the time range for the oscillations are shorter in Run 1 and Run 3 compared to Run 2.

Time	k_0 $[m^{-1}]$	λ_1 $[m]$	λ_{viz} $[m]$	u_{out} $[m/s]$	A_1/u_{out}
6.41 s	2.77×10^2	1.14×10^{-2}	-	6.93×10^{-1}	1.08×10^{-2}
6.42 s	3.53×10^2	0.89×10^{-2}	1.5×10^{-2}	6.90×10^{-1}	0.59×10^{-2}
6.43 s	2.34×10^2	1.34×10^{-2}	-	6.62×10^{-1}	2.76×10^{-2}
6.44 s	2.69×10^2	1.17×10^{-2}	1.2×10^{-2}	6.59×10^{-1}	2.24×10^{-2}
6.45 s	2.29×10^2	1.38×10^{-2}	1.2×10^{-2}	6.38×10^{-1}	2.31×10^{-2}
6.46 s	2.24×10^2	1.41×10^{-2}	1.2×10^{-2}	6.17×10^{-1}	1.17×10^{-2}

Table 3: $a/d = 0.292$ Run 1. Wave numbers k_0 and wavelengths λ_1 extracted from Fourier transformation, wavelengths λ_{viz} extracted manually from the figures, outer velocity u_{out} and amplitude A_1/u_{out}

5.3.3 Irregularities of $a/d = 388$ and $a/d = 0.481$

The largest waves with $a/d \sim 0.4$ and 0.5 were unstable during runup in the upper FOV. Attempts to find structures akin to Tollmien Schlichting waves have been made. Unfortunately, they failed due to poor seeding in the start of the runup tongue causing loss of velocity vectors in the early stage of the runup.

Fluctuations, but without good repeatability, were also detected for $a/d \sim 0.5$ in the FOV located close to equilibrium in the middle of the tank. The flow turned unstable in one out of four experiments. Video recordings revealed that the beach experienced a depression (up to 1 mm) during runup due to the load of the swash flow. However, at present it is not clear how this may cause pronounced transverse

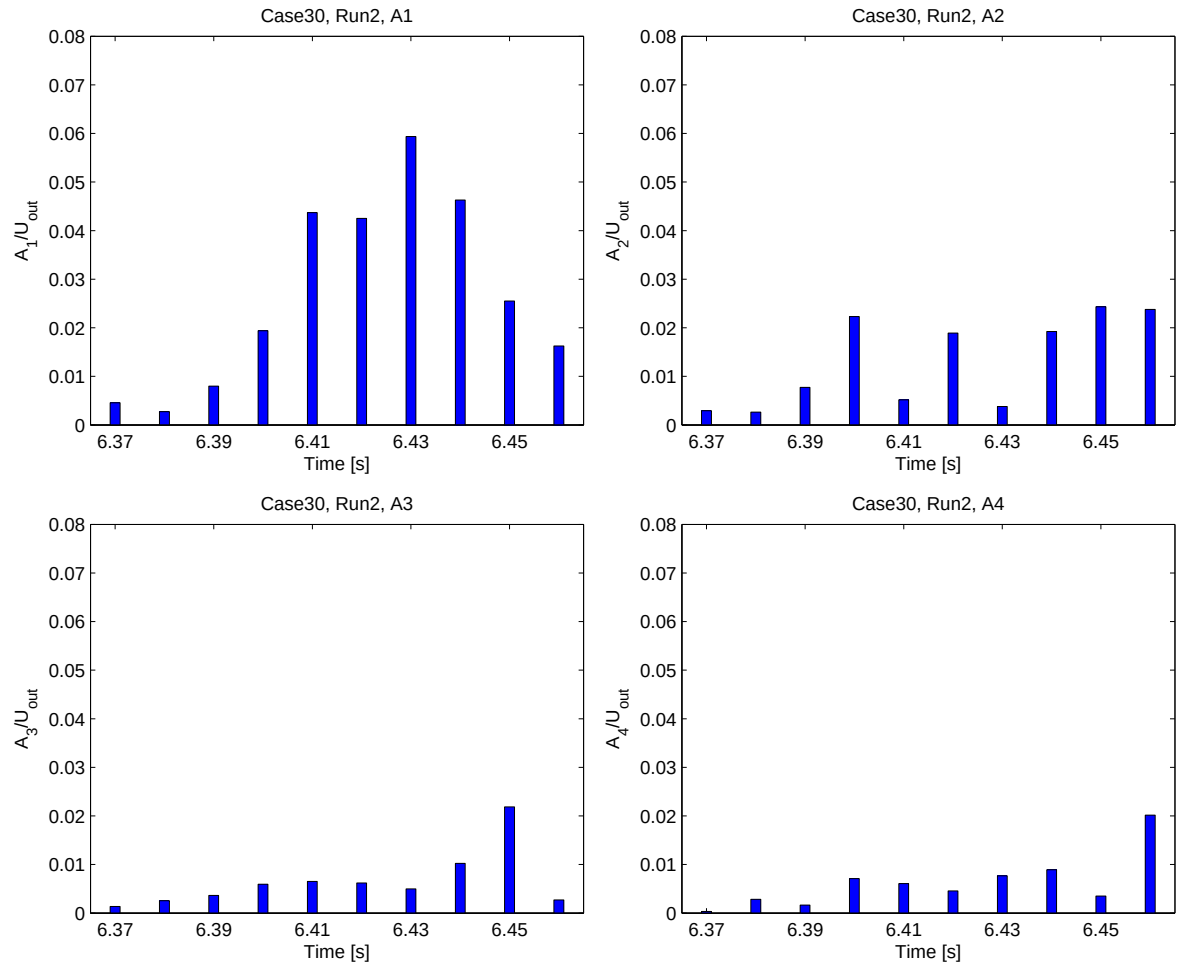

Figure 14: $a/d \sim 0.3$ Run 2. Growth in amplitude for k_1 (upper left), k_2 (upper right), k_3 (lower left), k_4 (lower right), $t = 6.37 - 6.46\,\mathrm{s}$.

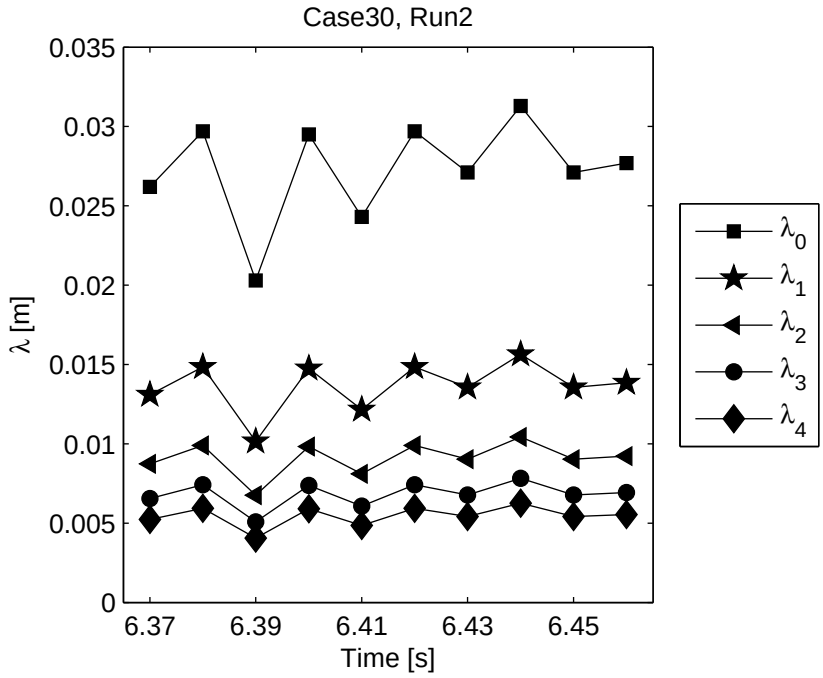

Figure 15: $a/d \sim 0.3$ Run 2. Wavelengths

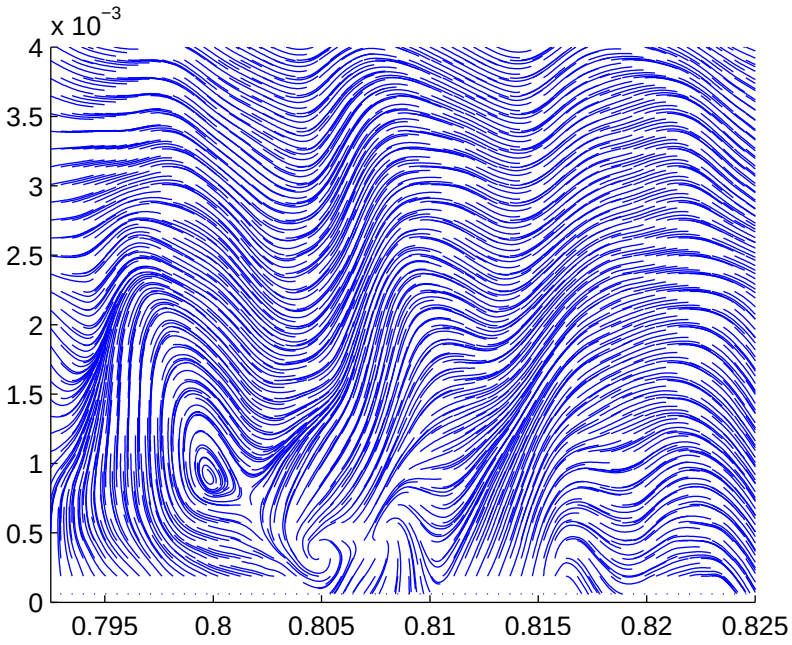

Figure 16: $a/d = 0.292$ Run 2. Streamlines with eddies at $t = 6.70\,\mathrm{s}$

Time	k_0 $[m^{-1}]$	λ_1 $[m]$	λ_{viz} $[m]$	u_{out} $[m/s]$	A_1/u_{out}
6.37 s	2.54×10^2	1.24×10^{-2}	1.2×10^{-2}	7.76×10^{-1}	2.90×10^{-2}
6.38 s	2.44×10^2	1.29×10^{-2}	1.5×10^{-2}	7.60×10^{-1}	4.69×10^{-2}
6.39 s	2.30×10^2	1.37×10^{-2}	1.2×10^{-2}	7.31×10^{-1}	4.41×10^{-2}
6.40 s	2.13×10^2	1.47×10^{-2}	1.2×10^{-2}	7.13×10^{-1}	4.30×10^{-2}
6.41 s	2.35×10^2	1.34×10^{-2}	1.3×10^{-2}	7.06×10^{-1}	4.30×10^{-2}
6.42 s	2.54×10^2	1.24×10^{-2}	-	6.92×10^{-1}	3.23×10^{-2}

Table 4: $a/d = 0.292$ Run 3. Wave numbers k_0 and wavelengths λ_1 extracted from Fourier transformation, wavelengths λ_{viz} extracted manually from the figures, outer velocity u_{out} and amplitude A_1/u_{out}

variation in the evolution of the boundary layers. In any case, the largest wave may be close to the transitional regime also in the start of the runup.

6 Remarks

[13] suggested that local instability is always to be expected in the decelerated parts of bottom boundary layers in transient or oscillatory flow. This is supported by the present theoretical investigation of instability in swash zone boundary layers. A crucial quantity from linear stability analysis for a flow of this type is the total amplification during the span of the unstable period. For a solitary wave in constant depth of 0.2 m this amplification is modest. It then decreases during shoaling while it is strongly increased, well beyond that in constant depth, in the swash zone, where we have large velocities and decelerations. Hence, in a runup experiment transition in the boundary layer are most likely to appear onshore.

It is to be expected that small scale features, such as undulatory behaviour in a boundary layer is, difficult to detect experimentally. From the experiments in [11] we could identify only one FOV in a single experiment with velocity measurement of sufficient quality for revelation of distinct flow patterns resembling Tollmien Schlichting waves. It is encouraging that for this experiment we found very good agreement for the time of appearance of instabilities and that the dominant length of the experimental undulations are close to the length of the critical Tollmien Schlichting waves. However, the realtive

growth rate of the observed waves cannot be reconciled with theoretical growth rates. Other repetitions of the same experiment suffered from poorer seeding leading to a lower quality in the measurements. Still, this is unlikely as a single explanation for the lack of reproducibility. Even though, irregular flow was observed in these repetitions as well, there were substantial differences in both amplitudes and the duration of the oscillations. According to [13] poor repeatability may be expected in such a case due to the nature of the instability and the absence of a controlled perturbation of the flow. To produce firm experimental evidence of the boundary layer instabilities in swash flow on this scale one would probably have to make a vast number of repetitions with well controlled sources of noise of different magnitudes. Moreover, according to, for instance, [4], a secondary instability may be expected when the magnitude of undulations reaches, say, 1% of that of the base flow. In our good experiment they reach 3-5% before vortex formation is observed and it is possible that the observed growth may be associated with the secondary rather than primary, linear instability. Methods like the PIV often have a noise level of order 1%, which makes direct observation of the first linear stage of the instability difficult in the first place.

References

[1] Paolo Blondeaux, Jan Pralits, and Giovanna Vittori. Transition to turbulence at the bottom of a solitary wave. *Journal of Fluid Mechanics*, 709:396–407, 2012.

[2] Paolo Blondeaux and Giovanna Vittori. Rans modelling of the turbulent boundary layer under a solitary wave. *Coastal Engineering*, 60:1–10, 2012.

[3] P. G. Drazin and W. H. Reid. *Hydrodynamic Stability*. Cambridge University Press, 1981.

[4] Thorwald Herbert. Secondary instability of boundary layers. *Annual Review of Fluid Mechanics*, 20:487–526, 1988.

[5] A. Jensen, G. Pedersen, and D. J. Wood. An experimental study of wave run-up at a steep beach. *J. Fluid. Mech.*, 486:161–188, 2003.

[6] R. Jordinson. The flat plate boundary layer. part 1. numerical integration of the Orr-Sommerfeld equation. *Journal of Fluid Mechanics*, 43:801–811, 1970.

[7] G. Sælevik. xxx, 2008. PhD thesis, University of Oslo.

[8] G. Sælevik, A. Jensen, and G. Pedersen. Runup of solitary waves on a straight and a composite beach. *Coastal Engineering*, 77, 2013.

[9] Celalettin E. Ozdemir, Tian-Jian Hsu, and S. Balachandar. Direct numerical simulations of instability and boundary layer turbulence under a solitay wave. *Journal of Fluid Mechanics*, 731:545–578, 2013.

[10] G. K. Pedersen, E. Lindstrøm, A. F. Bertelsen, A. Jensen, D. Laskovski, and G. Sælevik. Runup and boundary layers on sloping beaches. *Physics of Fluids*, 25:pp. 23, 2013. doi: 10.1063/1.4773327.

[11] Geir K. Pedersen, Erika Lindstrøm, Arnold F. Bertelsen, Atle Jensen, Daniela Laskovski, and G. Sælevik. Runup and boundary layers on sloping beaches. *Physics of Fluids*, 25:pp. 23, 2013.

[12] B. Mutlu Sumer, Palle M. Jensen, Lone B. Sørensen, Jørgen Fredsøe, Philip L.-F. Liu, and Stefan Carstensen. Coherent structures in wave boundary layers. part 2. solitary motion. *Journal of Fluid Mechanics*, 646:207–231, 2010.

[13] Joris C. G. Verschaeve and Geir K. Pedersen. Linear stability of boundary layers under solitary waves. *Journal of Fluid Mechanics*, under review.

[14] Giovanna Vittori and Paolo Blondeaux. Turbulent boundary layer under a solitary wave. *Journal of Fluid Mechanics*, 615:433–443, 2008.

[15] Giovanna Vittori and Paolo Blondeaux. Characteristics of the boundary layer at the bottom of a solitary wave. *Coastal Engineering*, 58:206–213, 2011.